Materials Today Bio 28 (2024) 101183

Contents lists available at ScienceDirect

Materials Today Bio

journal homepage: www.journals.elsevier.com/materials-today-bio

Novel multidomain peptide self-assembly biomaterials based on bola structure and terminal anchoring: Nanotechnology meets antimicrobial therapy

Weikang Yu, Xu Guo, Xuefeng Li, Yingxin Wei, Yinfeng Lyu, Licong Zhang, Jiajun Wang **, Anshan Shan *

College of Animal Science and Technology, Northeast Agricultural University, Harbin, 150030, PR China

ARTICLE INFO

Keywords:
Antimicrobial peptide
Self-assembly
Bola structure
Terminal anchoring
Antibacterial mechanisms

ABSTRACT

To ameliorate the diminished antimicrobial efficiency and physiological stability associated with monomeric antimicrobial peptides (AMPs) molecules, future research will focus on the artificial design of self-assembling peptides to replace monomeric entities, aiming to combat the antibiotic resistance crisis caused by microbial infections. In this study, the "bola" structure was used as the foundational architecture driving molecular self-assembly, with hydrophobic amino acids at the termini to anchor and finely adjust the sequence, thereby organizing a range of novel multidomain peptides (MDPs) templates into an ABA block motif. The results indicate that FW2 ($GM_{SI} = 53.94$) exhibits the highest selectivity index among all MDPs and can form spherical micelles in an aqueous medium without the addition of any exogenous additives. FW2 exhibited high stability in vitro in the presence of physiological salt ions, serum, and various pH conditions. It exhibited excellent biocompatibility and efficacy both *in vivo* and in vitro. Furthermore, FW2 strongly interacts with the lipid membrane and employs various synergistic mechanisms, such as reactive oxygen species (ROS) accumulation, collectively driving cellular apoptosis. This study demonstrates a straightforward strategy for designing self-assembling peptides and promotes the advancement of peptide-based biomaterials integration progress with nanotechnology.

1. Introduction

Antibiotic misuse has resulted in the escalating resistance of numerous bacterial strains, giving rise to a cascade of superbugs that pose a serious threat to human health [1,2]. Contemporary approaches to addressing antimicrobial-resistant (AMR) bacteria rely on the development of innovative antibiotics, the deployment of diverse antibiotic classes, and the use of antibiotic combinations [3,4]. Nonetheless, the process of natural selection acting on AMR strains is ongoing, with the potential to culminate in the emergence of multidrug resistant (MDR) microorganisms capable of undermining the efficacy of most antibiotic therapies. Consequently, there exists an imperative need to formulate effective antibacterial agents [5–8].

Antimicrobial peptides (AMPs), which are essential constituents of the innate immune response in multicellular eukaryotes, serve as the primary defense mechanism in the biological immune system against MDR bacteria. Due to their broad-spectrum antibacterial activity and reduced potential for resistance induction, AMPs have received significant attention as promising candidates for combating MDR bacteria [9–16]. However, the majority of AMPs exist as monomers, posing significant challenges including insufficient antimicrobial activity, non-specific targeting of bacterial and mammalian cell membrane components leading to cytotoxicity, and concerns regarding stability under physiological conditions due to exposed binding sites. These limitations significantly limit their clinical application [17–20].

Recently, it has been identified that amphiphilic structures form the structural foundation for AMPs activity, and enable peptides to undergo self-assembly, allowing them to spontaneously form specific structures through non-covalent interactions in aqueous environments or solutions under suitable conditions [11,17]. Unlike conventional AMP monomers, which interact with microbial membranes as individual molecules, peptide assembly can rapidly increase local concentrations to the

* Corresponding author.
** Corresponding author.
E-mail addresses: wjj1989@neau.edu.cn (J. Wang), asshan@neau.edu.cn (A. Shan).

https://doi.org/10.1016/j.mtbio.2024.101183
Received 26 March 2024; Received in revised form 28 June 2024; Accepted 3 August 2024
Available online 6 August 2024
2590-0064/© 2024 The Authors. Published by Elsevier Ltd. This is an open access article under the CC BY-NC license (http://creativecommons.org/licenses/by-nc/4.0/).

saturation point of the membrane, potentially enhancing their properties [19,21,22]. Furthermore, assembly can improve the physiological stability and biocompatibility of peptide-based biomaterials [14,19,23]. Future monomer AMPs may gradually be replaced by self-assembling AMP libraries with specific nanostructures [24,25]. Surfactant-like peptides (SLPs) composed of natural amino acids are particularly intriguing among the numerous types of self-assembling peptides due to their inherent biocompatibility and accessibility through conventional peptide synthesis [26–29]. The molecules are usually characterized by a single polar head containing hydrophilic amino acids and a long tail composed of nonpolar amino acids or hydrocarbon chains linked by ester bonds [30]. However, an interesting exception to this traditional single-headed layout in bola-amphiphiles, where two hydrophilic moieties flank a hydrophobic core [22,31]. Due to their double-headed design, bola-amphiphiles exhibit more complex aggregation phenomena than their single-headed counterparts [32]. Additionally, the bola structure demonstrates superior water solubility and thermal stability [33]. Briefly, compared to traditional amphiphilic and Gemini structures, the hydrophobic regions in the bola structure are concentrated internally, while the double-headed hydrophilic regions remain on the terminal surfaces, ensuring higher solubility [34]. This characteristic is particularly advantageous for constructing peptide-based biomaterials or self-assembling drugs. Additionally, the structural stability of bola structure and easily adjustable self-assembly properties have been widely applied in the biomedical field [28].

However, research on bola peptides has predominantly focused on forming hydrogels for hemostasis or as improved drug carriers, primarily due to its propensity to form β-sheet based ribbon structures [27,35]. The characteristic leads to relatively weak antimicrobial activity of bola peptides has limited their development and application in clinical therapeutics as antibacterial agents. Consequently, further research and strategies are required to enhance the antibacterial potential of the bola structure. One possible approach is to modify the bola structure by incorporating antimicrobial active groups or introducing chemical modifications. These modifications may involve the incorporation of molecular fragments with strong antibacterial activity to enhance the overall antibacterial effectiveness [36]. In light of these considerations, this study describes multidomain peptides (MDPs) featuring an ABA block motif, aiming to strike a balance between self-assembly-based drug delivery and antibacterial potential. The central B block consists of a bola structure composed of arginine (Arg, R) and hydrophobic amino acids (tryptophan (Trp, W) and phenylalanine (Phe, F). In conjunction with prior research, the use of hydrophobic labels as capping agents for peptides improves their antimicrobial efficacy and stability while avoiding toxicity escalation [37]. Therefore, its A block is anchored at the terminus by a single Trp or Phe.

Arg was selected as the positively charged core due to the enhanced affinity of AMPs for the surface of the membrane associated with its guanidyl side chain, resulting in potent bactericidal effect [22]. One of the essential prerequisites for membrane penetration is met by the presence of Trp, which can generate negatively charged electron clouds owing to the robust quadrupole moment exhibited by the π-electron system of aromatic residues, which can engage with cationic molecules, such as choline groups, within the bacterial lipid bilayer, leading to an extended association with the bacterial lipid membrane [36,38]. Moreover, aromatic Phe forms hydrophobic interactions with phospholipids, which contributes to their biological activity. Aromatic amino acids (F and W) were selected instead of aliphatic amino acids (V, I, and L), because aromatic amino acids have a stronger ability to enhance peptide self-assembly and membrane-disrupting ability [22].

In this study, the bola structure was used to establish a fundamental framework for the self-assembly of MDPs. A series of MDPs were designed by integrating hydrophobic amino acids to anchor the sequence terminals. MDPs integrates the amphiphilicity of AMPs, the self-assembly stability of bola structures, and the antimicrobial activity segments conferred by the terminal anchoring. The structural and functional links of these peptides were elucidated by fine-tuning the sequence positions of the aromatic amino acids, resulting in highly effective antimicrobial agent templates. FW2 was found to have the highest selectivity index (GM_{SI} = 53.94). Furthermore, FW2 can form spherical micelles in an aqueous media and exhibits excellent antimicrobial activity in vitro and in a mouse peritonitis-sepsis model. Due to the advantages of nanoscale structures, FW2 exhibits high stability in the presence of serum and physiological salts. Its primary mechanism of action involves membrane disruption, which is supported by a multimodal action mechanism, that drives bacterial cell death (Scheme 1). In summary, integrating nano systems with peptide sequences can facilitate the development of antimicrobial biomaterials and alleviate the antibiotic resistance crisis.

2. Materials and methods

2.1. MDPs production and characterization

Synthesis of the peptides was carried out by GL Biochem Ltd. (Shanghai, China). Matrix-assisted laser desorption/ionization time-of-flight mass spectrometry (MALDI-TOF MS; Linear Scientific Inc.) was used to determine peptide molecular weights. The Purity (>95 %) and retention time of the sample were determined via reversed-phase high-performance liquid chromatography (RP-HPLC) on a Gemini-NX-C18-110 A chromatographic column (4.6 × 250 mm^2, 220 nm). The mobile phase, which featured a nonlinear water/acetonitrile gradient with 0.1 % trifluoroacetic acid, facilitated a 20 μL sample load at a flow rate of 1.0 mL/min.

2.2. CAC assay

The 1-anilino-8-naphthalene sulfonate (ANS) fluorescence assay was utilized to determine the critical aggregation concentration (CAC) of the peptide [39]. Dimethylformamide (DMF) was used to dissolve ANS at 2 mM. In a 96-well plate, 100 μL of peptide solutions with different concentrations were mixed with 1 μL of ANS, and the solution mixture was analyzed with an F-4500 fluorescence spectrophotometer (Hitachi, Japan). With excitation at 369 nm, the fluorescence spectrum ranged from 420 to 550 nm. ANS fluorescence intensities at 475 nm were plotted against different peptide concentrations to calculate the CAC value.

2.3. Circular dichroism spectroscopy (CD) assay

The secondary structure of the peptide was analyzed using a CD spectrometer (Chirascan, U.K.) [19]. The spectra of the peptide (at 64 μM concentration) were measured in deionized water containing 30 mM sodium dodecyl sulfate (SDS) and 50 % trifluoroethyl alcohol (TFE) present.

2.4. Antimicrobial activity assays

The antimicrobial activities of the peptides were evaluated by a modified approach derived from the Clinical Laboratory and Standards Institute (CLSI) protocol [40]. To determine the minimum inhibitory concentrations (MICs), bacteria were cultured in an Mueller-Hinton broth (MHB) medium and adjusted to the required concentration (1 × 10^5 CFU/mL) [22]. The MDPs were mixed with bacterial suspensions at various concentrations and incubated at 37 °C for 18–24 h. Negative control involves using MHB without any bacteria. After incubation, a spectrophotometer was employed to determine absorbance at 492 nm. The MIC value was evaluated when the test exhibited clarity without turbidity. To assess the minimum bactericidal concentrations (MBCs), 10 μL of each transparent well solution was poured into an MHA plate and incubated at temperature of 37 °C for 24 h. Subsequently, the number of colonies was examined. MBC was defined as the drug

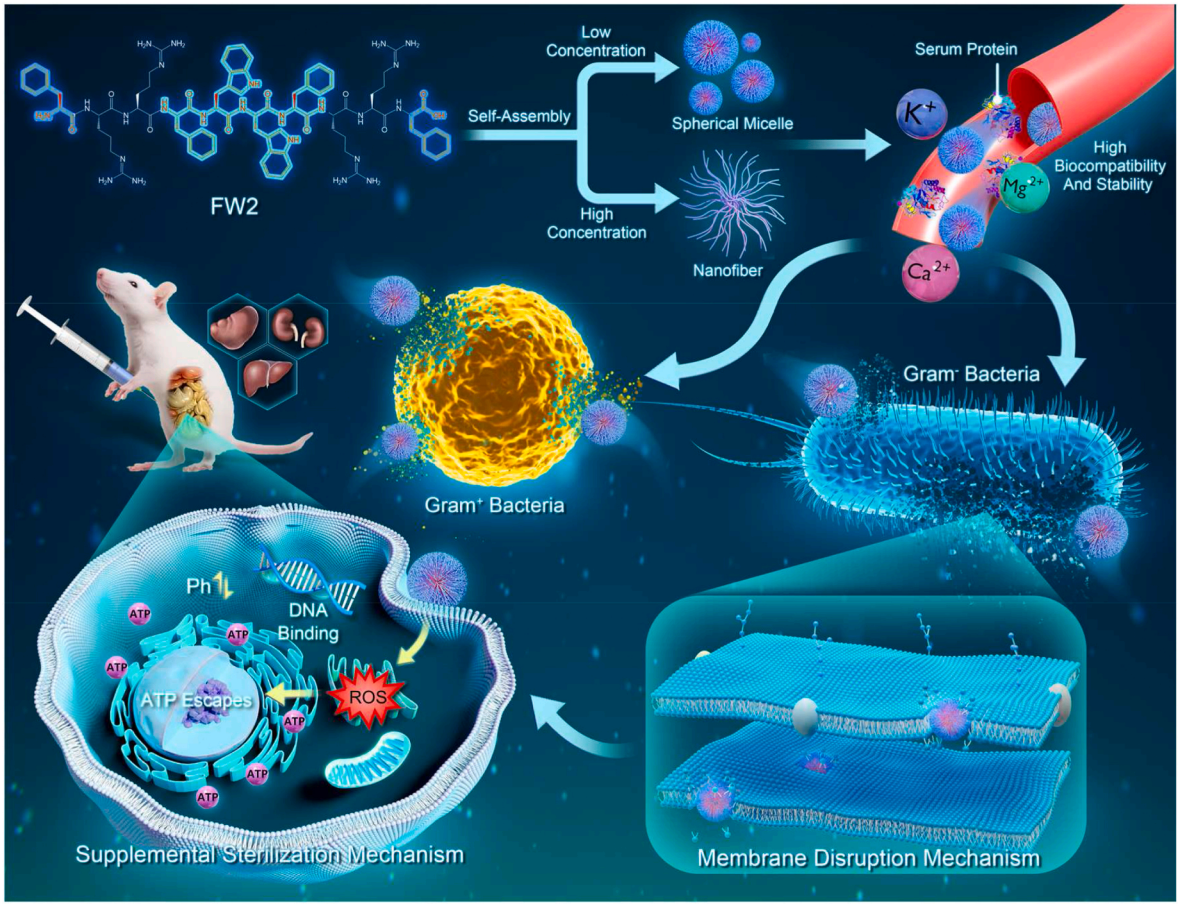

Scheme 1. Schematic illustration of the self-assembly peptide FW2 microstructural changes and its biological implications.

concentration that caused a 99.9 % decrease in bacterial viability. Three independent experiments were conducted, and each treatment was replicated three times.

2.5. Hemolysis assays

Human red blood cells (hRBCs) were obtained from healthy donors and stored at 4 °C in polycarbonate test tubes containing anticoagulants. A 10 min centrifugation at 1000*g* was performed on 1 mL hRBCs to remove the upper serum layer. The hRBCs were then resuspended in PBS (10 mM, pH 7.4) to approximately 2 % dilution (v/v). Different amounts of the peptides were added to a 96-well plate, with 50 μL of hRBCs solution. The mixture was then incubated at 37 °C for 1 h. For the positive control, hRBCs were treated with Triton X-100 (0.1 %, v/v), whereas the negative control consisted of untreated hRBCs. After incubation, the 96-well plate was centrifuged at 1000 *g* for 10 min. Subsequently, the upper phase (50 μL) was transferred to a new 96-well plate for quantifying released hemoglobin using a microplate reader (570 nm, Tecan GENios F129004, Austria). The findings were analyzed by Li's methodology [39].

2.6. Cytotoxicity assays

Mouse mononuclear macrophage (RAW 264.7) and human embryonic kidney (HEK 293T) cells were cultured in RPMI-1640, DMEM, and DMEM/F-12 containing high glucose, streptomycin sulfate (100 μg/mL), and penicillin (100 U/mL) [41]. Cells were subcultured until the entire bottom of the cell culture flasks with a capacity of 25 cm^{-2} were completely covered. Then, the cells were diluted to a concentration of 3 $\times 10^5$ cells per well and mixed with different peptide concentrations in a 96-well plate. Untreated cells and pure media served as both positive and negative controls. After 4 h of incubation with 5 % carbon dioxide at 37 °C, 3-(4,5-dimethylthiazol-2-yl)-2,5-diphenyltetrazolium bromide (MTT, 50 μL, 0.25 mg/mL) was added to each well, and the plates were again incubated for 4 h. The supernatant was removed, and the formazan crystals were dissolved in 100 μL of dimethyl sulfoxide (DMSO). The test was conducted three times separately, and the findings were calculated using Lai's approach [19].

2.7. Molecules dynamics (MD) simulation

The MD trajectory underwent analysis using the GROMACS software and Visual Molecular Dynamics (VMD) software. Previous study can be referred to achieve the experimental method used in this paper [42].

2.8. Observations on peptide self-assembly

For transmission electron microscopy (TEM), FW2 was dissolved in water to 4 μM, CAC, 128, and 256 μM (initial concentration of 2.56 mM). Incubation of the diluted mixture (CAC, 128 and 256 μM) took place at a temperature of 37 °C for 24 h. Additionally, the diluted solution (4 μM) underwent incubation at ambient temperature for 30 min. Afterward, the specimens were placed onto a carbon grid coated with a copper mesh of 300-mesh and stained with 1 % phosphotungstic acid for 30 s. Ultimately, the examination was conducted utilizing a Hitachi H-7800 TEM (Hitachi, Japan) that operated at a voltage of 100 kV.

2.9. Time kill kinetics assay

The logarithmic phase of *E. coli* ATCC 25922 or *S. aureus* ATCC

29213 was achieved through incubation, and the concentration was adjusted to approximately 1×10^5 CFU/mL using PBS (10 mM, pH 7.4). Subsequently, the bacteria were incubated with the peptide at a concentration of 1 × MBC. At different time, the samples were diluted and applied to MHA plate. After an overnight culture at 37 °C, samples were counted. To obtain precise outcomes, the experiment was conducted three times.

2.10. Dynamic light scattering (DLS) and zeta-potential assay

To evaluate the dynamic size and zeta potential of FW2 in the water-based solution, Zetasizer Nano Z90 (Malvern Instruments, Worcestershire, U.K.) was used. A disposable plastic cuvette was used to hold solutions with a concentration of 256 μM, CAC, and 4 μM. Three measurements were performed on each sample using a viscosity matching that of deionized water, a refractive index set for proteins, and a constant temperature of 25 °C.

2.11. Salt, serum, and pH sensitivity assays

The MIC values were determined by combining various concentrations of FW2 with physiological salts (NaCl (150 mM), KCl (4.5 mM), NH_4Cl (6 μM), $ZnCl_2$ (8 μM), $CaCl_2$ (2 mM), $MgCl_2$ (1 mM), and $FeCl_3$ (4 μM)). FW2 was cultured with 50 %, 25 %, and 12.5 % fetal bovine serum at 37 °C for 4 h. To evaluate the durability of FW2 under varying pH conditions, it was exposed to PBS (with pH levels of 2, 4, 10, or 12) at 37 °C for 4 h. Three replicates were conducted for each treatment, and the experiment was repeated independently three times.

2.12. Confocal laser scanning microscopy (CLSM) assay

FITC-labeled peptides (1 × MIC) were applied to *E. coli* ATCC 25922 and *S. aureus* ATCC 29213 cells ($OD_{600} \approx 0.3$) in HEPES buffer at 37 °C for 60 min. After another 30 min, propidium iodide (PI) (10 μg/mL) was added to the reaction mixture, and the unbound FITC dye was removed using a wash with HEPES buffer. A confocal laser scanning microscope (Leica TCS SP8, Germany) was used to analyze the suspended specimen.

2.13. Fluorescence microscope assay

To assess the viability of bacteria, a live/dead BacLight kit was used in combination with an EVOS FL Auto fluorescence microscope from the United States. To acquire $OD_{600} = 0.3$, *E. coli* ATCC 25922 and *S. aureus* ATCC 29213 in the mid-logarithmic growth phase were collected through centrifugation at 1000×*g* for 5 min. The collected cells were then diluted in HEPES buffer. FW2 was subsequently cultured with the sample for 1.5 h at 37 °C, after which SYTO9 and PI were introduced. A dual-color fluorescence background was achieved in microscope.

2.14. LPS and LTA binding assay

The affinities of FW2 was evaluated for LPS and LTA by employing a BODIPY-TR-cadaverine (BC) probe. The lipopolysaccharide (LPS) (50 μg/mL) derived from *E. coli* O111 B4 and lipoteichoic acid (LTA) (50 μg/mL) obtained from *S. aureus* were combined with BC (5 μg/mL) and incubated for 4 h in a lightless environment. Serial dilutions of peptides (50 μL) were made in Tris buffer (pH 7.4) utilizing 96-well plates, followed by the addition of the LPS/LTA-BC mixture to each well. In addition to the untreated negative control group consisting of 100 μL of LPS/LTA-BC mixture, a positive control treated with polymyxin B (20 μg/mL) was also incorporated. Fluorescence intensity was measured using a spectrophotometer at an excitation wavelength of 580 nm and an emission wavelength of 620 nm. Each test was conducted in three independent replicates. Subsequently, calculations were performed according to the method outlined by Shao and Lyu [43,44].

2.15. Outer membrane (OM) permeabilization assay

As outlined in Zhu's study [45], the N-phenyl-1-naphthylamine (NPN, Sigma-Aldrich) probe was used for the OM permeabilization assay. *E. coli* ATCC 25922 was selected as the experimental specimen. Using fluorescence spectrophotometer with 350 nm excitation and 420 nm emission wavelengths, background fluorescence was measured.

2.16. PG competitive inhibition assay

Phosphatidylglycerole (POPG) (50 μL) and FW2 (50 μL, 4 × MIC) were incubated at 37 °C for 1 h, following the procedure detailed in previous studies [42].

2.17. Membrane fluidity assay

As descripted in Kim's study [46], an overnight culture of *E. coli* ATCC 25922 and *S. aureus* ATCC 29213 cells were diluted to a concentration of 3×10^5 CFU/mL in HEPES buffer. The bacterial suspension was then incubated with Laurdan GP (2.5 mM) for 60 min at 37 °C in a dark environment. Following this, peptides of various concentrations, equaling a volume of 50 μL, were added and thoroughly mixed in plate. Benzyl alcohol (BA) (3 mM) served as the positive control. Laurdan fluorescence intensities were assessed using an F-4500 fluorescence spectrophotometer (Hitachi, Japan) with an excitation wavelength of 492 nm and emission wavelengths of 435 nm, maintaining a temperature of 37 °C. The calculation of Laurdan GP was performed using the formula $GP = (I_{435} - I_{490})/(I_{435} + I_{490})$.

2.18. Cytoplasmic membrane (CM) potential assay

3,3′-dipropylthiadicarbocyanine ($DiSC_3$-5) was used to assess bacterial CM potential [47]. *E. coli* ATCC 25922 or *S. aureus* ATCC 29213 were diluted to $OD_{600} = 0.05$ in HEPES buffer. Following this, a final concentration of 0.5 μM $DiSC_3$-5 was introduced into the bacterial suspension and incubated in darkness for 90 min. Upon combining the bacterial suspension with the different concentrations of peptide solution. Subsequently, the alteration in fluorescence was assessed using a microplate reader at an excitation wavelength of 620 nm and an emission wavelength of 670 nm.

2.19. Permeabilization assay of inner membrane (IM)

The assessment of IM permeability alterations in Gram-negative bacteria was conducted using the ONPG method [14]. *E. coli* ATCC 25922 cells were cultured until reaching mid-logarithmic phase in MHB supplemented with 2 % lactose. Subsequently, *E. coli* ATCC 25922 cells were diluted to an OD_{600} of 0.1 in HEPES buffer (pH 7.4) and *o*-nitrophenyl-*β*-D-galactopyranoside (ONPG) (1.5 mM). The compound FW2 was serially diluted in sterile 96-well plates, followed by the addition of an equivalent volume of bacterial suspension. Measurements of OD_{420} were taken over a duration of 100 min, starting from the initial time point.

2.20. Respiratory chain inhibition assay

E. coli ATCC 25922 or *S. aureus* ATCC 29213 cells in mid-logarithmic phase were diluted to an $OD_{600} = 0.4$ in Tris buffer (pH 8.6). Next, an equal combination of red tetrazolium (RT) (1 mg/mL), Glucose (100 mM), and Tris Buffer was prepared. Subsequently, varying concentrations of peptides were introduced into the mixture, followed by the addition of an equal volume of bacterial suspension. OD_{492} measurements were promptly taken after 60 min of incubation at 37 °C.

2.21. SEM and TEM assay

Bacteria were centrifugated and re-suspended to an $OD_{600} = 0.3$ in HEPES buffer. Following this step, the bacterial suspension was incubated with peptides (at a final concentration of 1 × MIC) for 60 min at 37 °C. Subsequently, the samples underwent centrifugation to eliminate the supernatant, and the bacteria were transferred to 1.5 mL tubes. Glutaraldehyde (2.5 %, w/v) was added and left overnight at 4 °C. The preparation of both SEM and TEM samples adhered to the procedure outlined by He et al. [37].

2.22. ATP leakage assay

Extracellular ATP levels in *E. coli* ATCC 25922 and *S. aureus* ATCC 29213 were assessed employing the Enhanced ATP Assay Kit (Beyotime, catalogue no. S0027). The assay was initiated by harvesting mid-log-phase *E. coli* and *S. aureus* cells, followed by dilution to $OD_{600} = 0.3$. Subsequently, bacterial cells were exposed to various concentrations of peptides and incubated for 90 min at 37 °C. Post-incubation, bacterial cells underwent centrifugation at 12,000 rpm for 10 min at 4 °C. The resulting bacterial precipitates were lysed utilizing lysozyme (20 mg/mL), followed by a further centrifugation step to acquire intracellular ATP. Luminescence measurements of the samples were conducted utilizing a spectrofluorophotometer.

2.23. DNA binding assay

As outlined in Lai's report [48], the process entailed the isolation of total genomic DNA utilizing a DNA extraction kit. Briefly, the peptide samples were mixed with the extracted complete genomic DNA from *E. coli* ATCC 25922 and *S. aureus* ATCC 29213 in a mixture of binding buffer, which consisted of 8 μL. Afterward, the mixtures underwent incubation at a temperature of 37 °C for a duration of 1 h. After the incubation period, the DNA loading buffer of the original source was added, and the samples were analyzed using 1 % agarose gel electrophoresis in a 0.5 × TFE buffer.

2.24. ROS generation assay

E. coli and *S. aureus* cells were gathered, washed in HEPES buffer, and subsequently diluted to $OD_{600} = 0.3$. After that, DCFH-DA was added to the mixture until it reached 200 μM. The solution was then incubated at 37 °C for 60 min. Afterward, the solution was gradually diluted in HEPES buffer to different levels of peptide concentration within a 96-well plate. The same volume of bacterial cells labeled with probe was included, and then incubated for an extra 30 min. The spectro fluorophotometer was employed to promptly monitor the fluorescence intensity at excitation $\lambda = 488$ nm and emission $\lambda = 525$ nm.

2.25. Intracellular pH assay

E. coli and *S. aureus* cells underwent washing and resuspension in HEPES buffer, followed by dilution to $OD_{600} = 0.3$. Post this step, the fluorescent probe BCECF-AM was incorporated into the medium, achieving a final concentration of 20 μM. Once fluorescence stabilization was attained, FW2 at diverse concentrations were added. The excitation wavelength was maintained at 488 nm, while the emission wavelength was set at 522 nm.

2.26. In vivo toxicity assay

Twenty-four healthy female ICR mice (6–8 weeks old) were allocated into four groups (6 mice one group). These mice were provided with common standardized basal diets and deionized water at an appropriate temperature and allowed to acclimate for 7 days. The control group of mice received intraperitoneal injections of saline, whereas the mice in the remaining three groups were administered FW2 (5, 10, and 20 mg/kg) intraperitoneally for a duration of 3 days. During the assessment period, variations in body weight were consistently observed. On the fourth day, euthanasia was performed under mild ether anesthesia [39]. Blood levels of serum biochemicals were assessed by collecting blood from the orbital veins of mice. Relative organ weight was measured by removing and weighing the liver, spleen and kidney. Morphological investigations involved fixation in 4 % paraformaldehyde, followed by staining with histological examination (H&E) for microscopic analysis.

2.27. Resistance development assay

Using sequential culturing, bacterial resistance to FW2 was assessed. Briefly, the MIC method was employed to ascertain the inhibitory concentration of FW2 against *E. coli* ATCC 25922. Fresh MHB broth was used for subsequent MIC method after retrieving the bacterial suspension from the sub-MIC well. For each assessment, MIC values were documented for up to 25 consecutive cycles.

2.28. In vivo efficacy assay

Female ICR mices (6–8 weeks) were chosen, with 8 mice allocated one group. Following a 3-day acclimatization period, the mice received an intraperitoneal injection of 100 μL suspension of *E. coli* cells diluted with saline ($OD_{600} = 0.3$) [49]. At 1 h and 4 h post-infection, mice were administered 10 mg/kg of FW2, 3 mg/kg of gentamicin, and saline, respectively. After infection, the mice were euthanized. Initially, 5 mL of saline was injected into the peritoneum to collect peritoneal cavity fluids through gentle massage and aspiration. A serum cytokine level assessment was conducted using blood samples. Liver, kidney, and spleen sections were stained with H&E, while the remaining organ parts were weighed, rinsed in saline, and homogenized. Following homogenization, the tissue was diluted appropriately and spread on MHA pre-prepared for overnight incubation at 37 °C.

2.29. Animal ethical principles

Animal care and treatment adhered to the National Research Council's Guide for the Care and Use of Laboratory Animals, and were approved by the Animal Research Ethics Committee, Northeast agricultural University, Harbin, China. The sex of the mice, whether male or female, has no impact on this study. However, gender consistency should be maintained.

2.30. Statistical analysis

GraphPad software is used to display numerical data as mean values with standard deviations (SD). Statistical evaluations were conducted employing either one-way ANOVA with Tukey's post hoc analysis. Significance was established at a threshold of $P < 0.05$. All experiments were replicated independently a minimum of three times.

3. Results and discussion

3.1. Design and self-assembly ability of MDPs

Six MDPs were synthesized by combining modified bola frameworks with a single hydrophobic amino acid end-tag to balance self-assembly and antibacterial potential. In this study, the four Arg residues were rationally placed in the hydrophilic region of the bola structure. The decision not to increase the number of positive charges was primarily based on the consideration that excessive hydrophilicity can lead to the breakdown of the self-assembled structure and an unnecessary reduction or loss of biological activity beyond the hydrophilic threshold [45]. Phe and Trp were then introduced into the entire hydrophobic region of the bola structure (altering the sequence positions of amino acids), and

anchored at the terminal of the peptide chain. Analogous to traditional alanine scanning techniques [50], this approach is used to investigate the critical role of specific aromatic amino acids in the hydrophobic regions of the bola structure or at the termini of peptide chains, including determining the optimal hydrophobicity values and hydrophobic moments to meet the requirements for antimicrobial activity and self-assembly propensity. The sequence template was XRRXXXXRRX-NH_2, where X represents F or W, and C-terminal

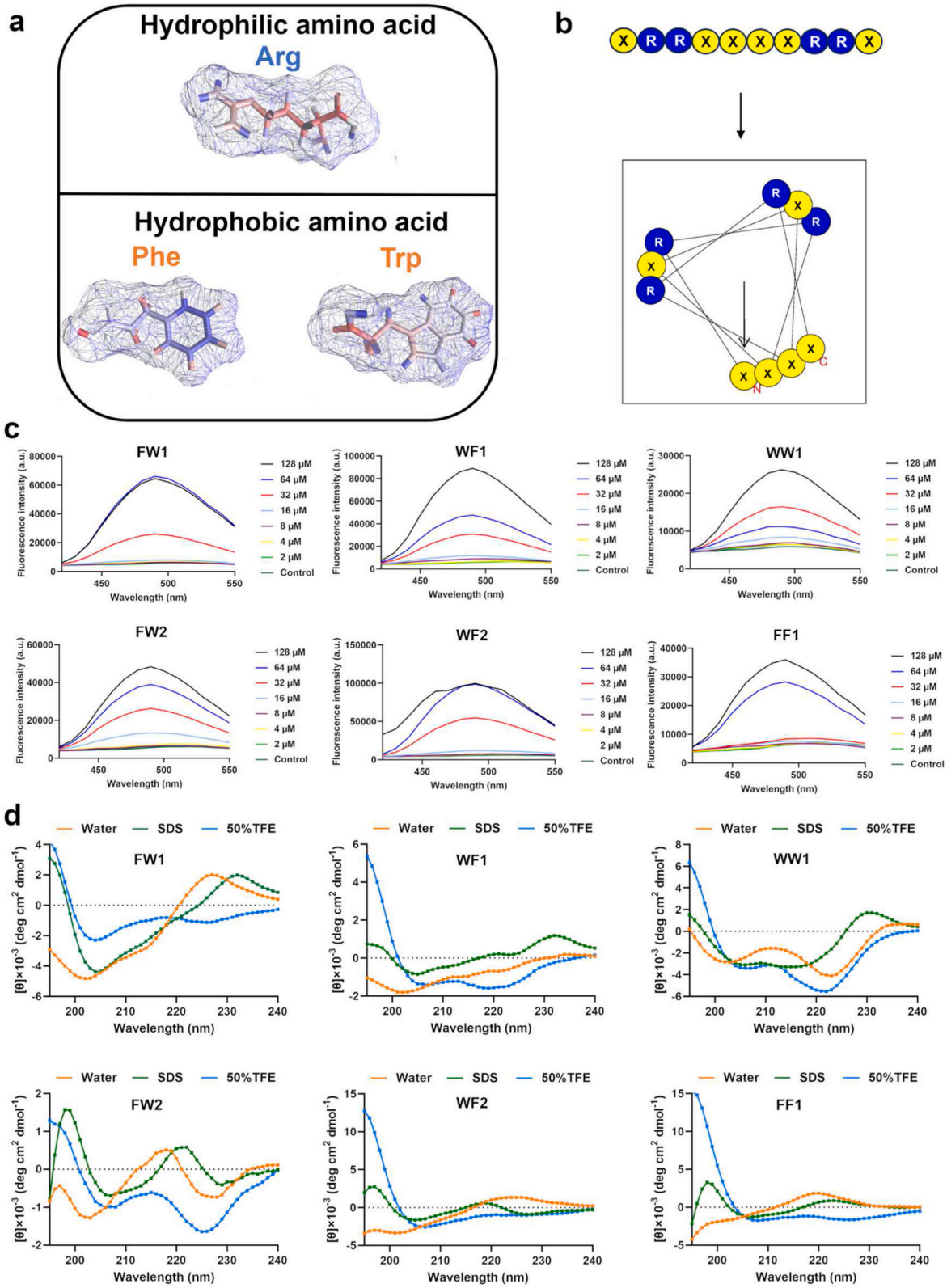

Fig. 1. (a) Composition of selected hydrophilic and hydrophobic amino acids. **(b)** Amphiphilic framework and helical wheel of MDPs based on the bola structure and terminal anchoring. **(c)** 1,8-ANS fluorescence emission intensity of the MDPs. **(d)** CD spectra of all peptides.

amidation of the peptide sequence was applied (Fig. 1a and Table 1).

As revealed in Table 1, the hydrophobicities of the MDPs remained between 0.670 and 0.946, while the hydrophobic moments were maintained between 0.693 and 0.923. The experimental molecular weights closely matched the theoretical molecular weights as illustrated in Figs. S1 and S2, for RP-HPLC and MALDI-TOF MS analyses of the MDPs, respectively. Additionally, all peptides exhibited a synthetic purity exceeding 95 %, affirming the successful synthesis of these compounds. Fig. S3 showed the chemical structures of the MDPs.

The self-assembly capacity and CAC value were assessed using a ANS fluorescence assay, which was employed because the fluorescence intensity increases with macromolecule binding [39]. It is well-established that AMPs in close proximity to the CAC can generate localized concentrations, thereby initiating and enhancing membrane interactions beyond the threshold required for membrane disruption [51]. Therefore, exploring the aggregation behavior of peptides in aqueous solutions is essential for sterilization. According to the helical wheel analysis, stacking four X residues together provides hydrophobic regions for the self-assembly system (Fig. 1b). Additionally, cation-π interactions represent another significant driving force for peptide self-assembly. Observations of all MDPs revealed a significant blue shift in fluorescence intensity with increasing concentration, indicating the ability of peptides to accumulate at low concentrations, and form larger aggregates as their concentration increases (Fig. 1c). The CAC values are given in Fig. S4 and Table 1.

Numerous studies have shown that an organized secondary structure is essential for the formation of nanostructures [14,18,20]. CD was used to investigate the conformational inclinations of peptides in diverse simulated settings (Fig. 1d). In an aqueous environment, different conformational tendencies were observed. The significant contribution of Trp at A block (sequence terminus) and central motif to supramolecular helical coils formation was noted [43,52]. Therefore, FW1 and WW1 displayed strong α-signals, exhibiting double negative peaks around 208 and 218 nm. Substituting Phe for Trp in A block while retaining the central Trp-Trp motif resulted in FW2 exhibiting dual signals for β-sheet and α-helix, with an additional positive peak at approximately 196 nm. When both Trp at the A block and the central Trp-Trp motif were substituted with Phe, WF2 and FF1 only displayed β-signals, without any observed feedback for α. Despite the retention of Trp at A block and substitution of central Trp-Trp motif with Phe-Phe, WF1 showed a weaker α-helix signal than FW1, as indicated by reduced absorption around 218 nm. Unlike the disordered conformation of monomeric peptides in aqueous solutions [53], the formation of self-assembled components relies on the support of ordered secondary structures in aqueous solutions. Except for WF2 and FF1 transitioning from β-turn to β-sheet, the conformations of the remaining peptides in SDS (Simulated negatively charged membrane) resemble those in aqueous solutions, indicating that the structural organization of the assembly components on the membrane surface may not exhibit excessive transient changes. However, in a 50 % TFE helix-inducing agent, all peptides were further organized into ordered α-helical structures.

3.2. Balancing of MDP screening in terms of antimicrobial activity and biocompatibility

The optimal screening of MDPs involves a complex and dynamic assessment of systemic effectiveness, along with the connection between antimicrobial efficacy and biocompatibility. The in vitro antimicrobial characteristics of MDPs were assessed using a representative assortment of pathogenic microorganisms. The use of MICs, MBCs and geometric mean (GM) facilitated the intuitive optimization of candidate sequences (Fig. 2a and Fig. S5). It was observed that peptides with the same bola domain showed GM_{MIC} values in the order FW2 < FW1 and WF2 < WF1 (Table 2). Furthermore, when compared to FW2 and WF2, FW1 and WF1 showed a small decrease in antimicrobial activity against *P. aeruginosa* and *S. typhimurium*, respectively. This suggests that the Phe-anchored structure at both termini gives the peptides higher antibacterial potency and a broader antibacterial spectrum. In contrast, when the anchoring domains were consistent, the Trp zipper at the molecular core played a significant role in enhancing antimicrobial activity compared with the FF core (FW1 < WF1 and FW2 < WF2). Previous research, has shown that Trp zippers provide stronger stacking stability than other aromatic and aliphatic amino acids in the same category. This may increase the contact area and insertion depth between AMPs and membrane components [22,54]. This was further demonstrated by comparing WW1 with FF1. WW1 possesses a stable double Trp zipper, resulting in a lower GM_{MIC} value than FF1. Taken together, FW2, with the dual characteristics of a core Trp zipper structure and a double-ended Phe -anchoring structure exhibited the highest biological activity, surpassing even Melittin.

Cytotoxicity is a crucial factor in the clinical translation of AMPs. As a result, the cytotoxicity of the peptides was then assessed against hRBCs cells (Fig. 2b), RAW 264.7 cells (Fig. 2c), and HEK 293T cells (Fig. 2d). The hemolysis baseline was established at 15 % hRBC lysis, while the baseline for mammalian cytotoxicity was defined as an 80 % cell survival rate. Except for a significant elevation in melittin toxicity toward hRBCs and other cell types, all peptides demonstrated minimal or negligible toxicity. One theory explaining this phenomenon is the difference in membrane structure between prokaryotic and eukaryotic cells. Most anionic components in the prokaryotic cell membrane are oriented toward the membrane surface, facilitating electrostatic interactions with the peptides. Conversely, in eukaryotic cells, most of the anionic components in the membrane face the interior [55]. Consequently, the peptides can selectively hinder bacterial growth while preserving eukaryotic cells. Combining biosafety and biological activity assessments, the calculated GM_{SI} value indicated that the optimal FW2 peptide (53.94) held a superior status. Hence, the subjective decision to use FW2 to investigate a series of subsequent indicators.

3.3. Analysis of the self-assembly morphology and physiological stability of FW2

A molecular simulation program was initially used to compute the characteristic parameters of the peptide, assess the propensity of FW2 to aggregate in aqueous solutions at the microscopic level, and investigate

Table 1
Physicochemical parameters and CAC value of peptides.

Peptides	Sequence	Theoretical MW	Measured MW	Hydrophobicity (H)	Hydrophobic moment (μH)	Purity	Charge	CAC (μM)
FW1	WRRFWWFRRW-NH_2	1680.97	1680.96	0.854	0.785	97.5 %	+4	14.48
WF1	WRRWFFWRRW-NH_2	1680.97	1680.96	0.854	0.923	98.2 %	+4	22.61
WW1	WRRWW W WRRW-NH_2	1759.04	1759.03	0.946	0.877	95.8 %	+4	12.08
FW2	FRRFWWFRRF-NH_2	1602.90	1602.88	0.762	0.693	96.8 %	+4	10.40
WF2	FRRWFFWRRF-NH_2	1602.90	1602.88	0.762	0.831	95.6 %	+4	11.48
FF1	FRRFFFFRRF-NH_2	1524.82	1524.81	0.670	0.739	96.4 %	+4	29.36
Melittin	GIGAVLKVLTTGLPALISWIKRKRQQ-NH_2	2846.49	2846.47	0.511	0.394	97.2 %	+5	No

Table 2
Summary of in vitro antimicrobial activity, biocompatibility, and selectivity index (SI) of MDPs.

Peptide	GM_{MIC}[a]	HC_{15}[b]	IC_{20}[c]		SI[d]			GM_{SI}[e]
		hRBCs	RAW264.7	HEK293T	hRBCs	RAW264.7	HEK293T	
FW1	8.93	256	128	128	28.67	14.33	14.33	18.06
WF1	12.39	256	128	128	20.66	10.33	10.33	13.01
WW1	5.76	256	128	128	44.44	22.22	22.22	28
FW2	**2.99**	**256**	**128**	**128**	**85.62**	**42.81**	**42.81**	**53.94**
WF2	5.16	256	128	128	49.61	24.81	24.81	31.26
FF1	8.00	256	128	128	32	16	16	20.16
Melittin	3.86	4	2	2	1.04	0.52	0.52	0.66

[a] GM_{MIC}: geometric mean of the MIC values against Gram-negative and Gram-positive bacteria.
[b] HC_{15}: The minimum concentration of the peptide that induces 15 % hemolysis of erythrocytes. When HC_{15} is greater than 256 μM, the SI value was determined using the value of 256 μM.
[c] IC_{20}: refers to the minimum peptide concentration that induces at least 20 % cell death, When IC_{20} is greater than 128 μM, the SI was determined using the value of 128 μM.
[d] SI: SI was calculated as HC_{15}/GM_{MIC} or IC_{20}/GM_{MIC}. A higher SI value indicates stronger cell selectivity.
[e] GM_{SI}: geometric mean of SI values.

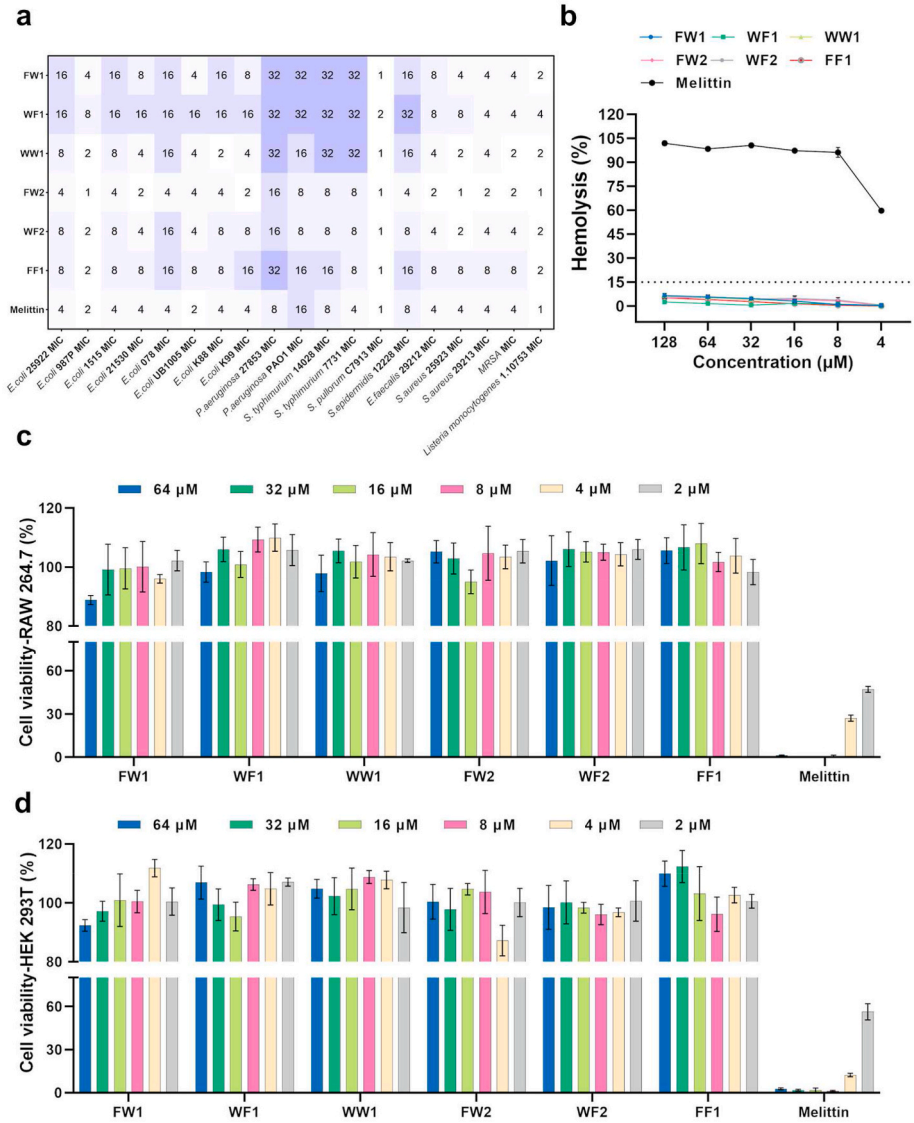

Fig. 2. **(a)** The MICs of the peptides against tested bacteria. **(b)** The hemolytic activity of peptides against hRBCs. The data presented as the mean ± SD; n = 3. **(c)** Cytotoxicity of various concentrations of the peptides against RAW264.7 cells and **(d)** HEK293T cells (mean ± SD, n = 3).

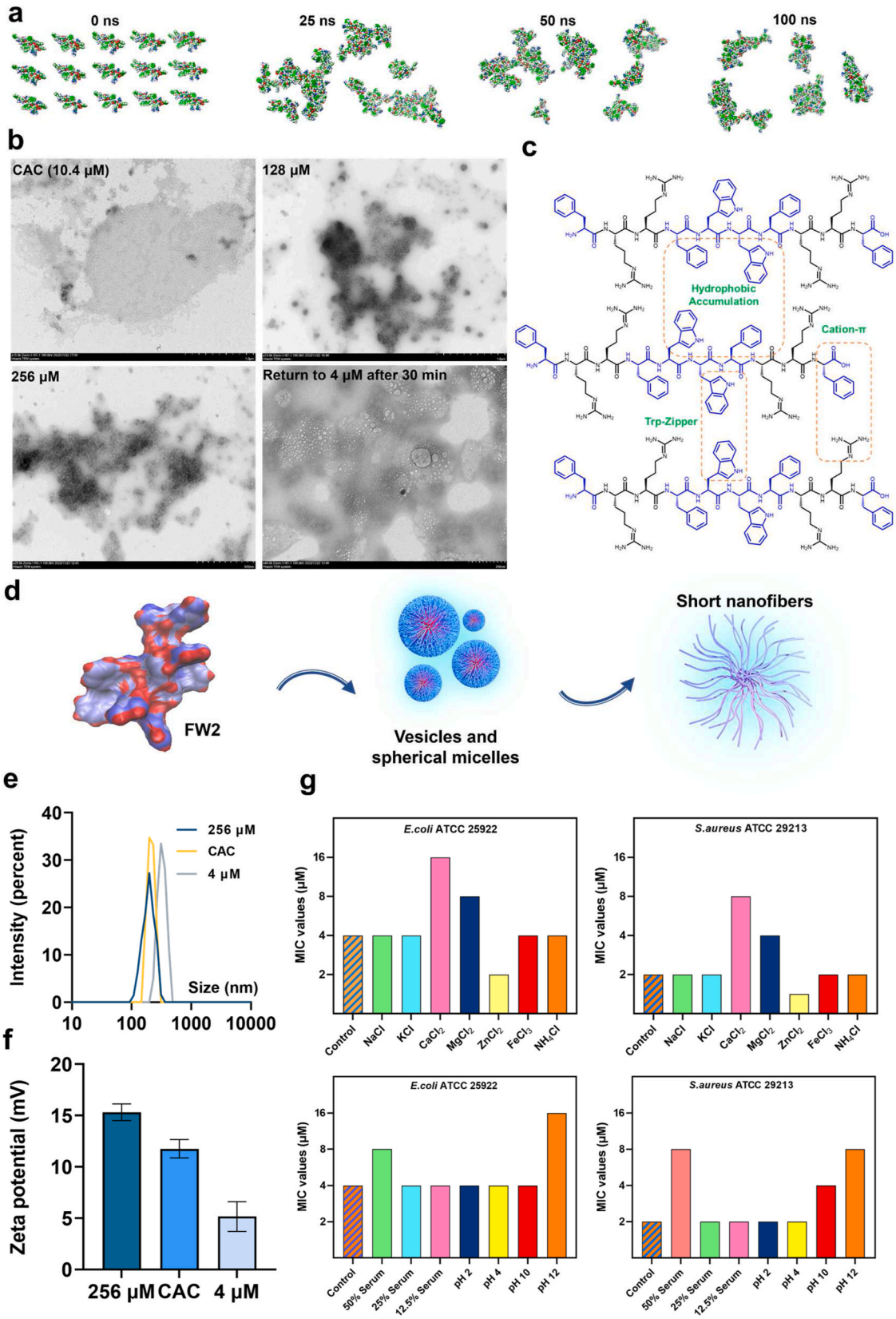

Fig. 3. **(a)** MD simulations of FW2 in an aqueous environment, images were acquired at 0, 25, 50, and 100 ns intervals. **(b)** TEM image of FW2 in an aqueous solution, maintaining concentrations at CAC, 128, 256, and 4 μM (stable at room temperature for 30 min). **(c)** Conceptual graphs of the main self-assembled driving force of FW2. **(d)** Schematic representation of the nanomorphological changes of FW2 monomeric molecules at various concentrations. **(e)** Determination of particle diameter and **(f)** Zeta potential of FW2 at different concentrations in an aqueous solution, data are presented as the mean ± SD; n = 3. **(g)** Variation in the MIC of FW2 in the presence of salt ions, serum, and pH. The experiment was replicated three times with three repetitions per group, to ensure consistent data across each set.

the details of the internal dynamics of FW2 molecules over a time span of 100 ns. Fig. 3a shows that the aggregation of FW2 molecules occurred within at least 25 ns because images acquired at 25, 50, and 100 ns demonstrated irregular but similar aggregation patterns. The root mean square deviation (RMSD) serves as a measure of structural consistency pre- and post-simulation [56]. Conformational disturbances in the assemblies were observed only around 0–10000 ps, with the attainment of a constitutionally stable structure occurring at approximately 15000 ps (Fig. S6). Similarly, it was observed that the radius of gyration (R_g) and solvent-accessible surface area (SASA) exhibit a rapid decrease and subsequent stabilization at approximately 10,000 ps (Figs. S7 and S8). This trend suggests that the molecular structure of FW2 undergoes densification, resulting in closer interactions among its constituents. Subsequently, TEM was employed to visually observe the nanostructures of FW2. Vesicles and spherical micelles of various sizes were also observed in CAC (Fig. 3b). At 128 and 256 μM, a larger number of short fibers were detected. It can be inferred that the assembly components formed by terminal anchoring of Phe and bola structures are concentration-dependent, leading to the diversity of the nanostructures. The heterogeneity and diversity of nanostructures offer possibilities for the morphological transformation of self-assembled AMPs to adapt to the affinity effects of different bacteria [22]. To assess the structural stability of FW2, 2.56 mM FW2 was uniformly dispersed in an aqueous solution to a final concentration of 4 μM (below CAC, close to MIC) and maintained at room temperature for 30 min. The continued presence of numerous spherical micelles and vesicles indicates the dynamic nature of the disassembly process of peptide, as it remains at least partially assembled and incompletely disaggregated into monomeric forms after 30 min. Since FW2 (1 × MBC) can kill 99.9 % of *E. coli* ATCC 25922 or *S. aureus* ATCC 29213 within 60 and 900 s, respectively, indicating the potential adoption of a spherical assembly configuration to target bacterial membranes (Fig. S9).

The self-assembly of FW2 is theoretically governed by hydrophobic forces, Trp zippers, cation-π interactions, and hydrogen bonds. Initially, the presence of hydrophobic groups results in stronger repulsion between water molecules than attraction, causing FW2 molecules to aggregate due to van der Waals forces [27]. At low concentrations, weak interactions between peptide molecules may result in the formation of structures with high curvature, stabilizing the dispersion of vesicles or micelles in water. As the concentration increases, due to the increased trends of molecule interaction, FW2 molecules exhibit a tendency toward lateral extension along the molecular axis, which is stabilized by Trp zippers, cation-π interactions, and π-stacking between N-terminal and C-terminal Phe (Fig. 3c). At this point, FW2 maintains both a spherical shape and a fibrous form (Fig. 3d). DLS was used to analyze the nanoparticle distribution within a solution, facilitating the assessment of their homogeneity, encompassing the water layer surrounding the nanoparticles within the specified calculation range [22]. With increasing concentration from 4 μM to 256 μM, the mean diameter of the particle micelles decreased from approximately 324 nm–196 nm, indicating an increase in intermolecular forces and coalescence of the micelles into a more compact spheroid or fibrous structure (Fig. 3e). Zeta potential measurements indicated a direct correlation between the surface charge of the assemblies and their concentration, which is essential for AMPs to attain systemic effectiveness while retaining electrostatic attraction to anionic microbial membranes (Fig. 3f).

Self-assembled structures enhance stability under physiological conditions [19]. Further investigations were conducted to assess its correlation with physiological salt ions, serum, and pH (Fig. 3g). Monovalent cations (Na^+ and K^+) that the electrostatic shielding effect exhibited no influence on FW2, suggesting that the increased contact area between the self-assembled entity and the membrane surface counteracted the negative impact of charge shielding [29]. The unsatisfactory data mainly focused on Ca^{2+}, which competitively binds to the LPS and LTA of the microbial surface, increasing membrane rigidity, and decreasing antimicrobial activity [57]. Nonetheless, the increased antimicrobial efficacy observed in FW2 treated with Zn^{2+} suggests that peptides may have a pre-covalent interaction with Zn^{2+} ions, stimulating their self-assembly and augmenting their adsorption efficiency onto microbial membranes [58]. Under assembly conditions, FW2 partially evaded serum protein binding sites, enabling the maintenance of significant activity even in the presence of 50 % serum, with only a 2–4 fold change in MIC value, while maintaining initial antimicrobial activity at serum concentrations of 25 % and 12.5 %. Furthermore, a slight decrease in antimicrobial activity was observed at pH 12 for both *E. coli* ATCC 25922 and *S. aureus* ATCC 29213, with a 4- fold increase in MIC value, potentially due to deprotonation of Arg side chains in an alkaline environment, leading to adverse effects on electrostatic attraction to the membrane surface [59]. However, antimicrobial activity remained intact at pH 2, 4, and 10, indicating the capability of FW2 to withstand alterations in *in vivo* microenvironments while maintaining efficacy.

3.4. Exploration of the preliminary cell membrane mechanisms of self-assembled peptide FW2

Similar to most monomeric natural peptides or engineered AMPs, it is hypothesized that FW2 micelles exhibit membrane-disruptive properties. A series of membrane perturbation assays were performed using representative Gram-negative bacteria, such as *E. coli* ATCC 25922, and Gram-positive bacteria, such as *S. aureus* ATCC 29213, as model organisms. Initially, CLSM was used to visualize the interaction of FW2 with the bacterial membrane surface. The FITC-labeled conjugated peptide exhibited green fluorescence, while PI entering damaged membrane cells exhibited red fluorescence (Fig. 4a and 4a-1). The LIVE/DEAD assay yielded analogous findings: with the introduction of SYTO 9, the micelle-induced membrane impairment led to the progressive overlap of SYTO 9 staining with the red signal emitted by PI, resulting in a merged chartreuse coloration (Fig. S10). These observations suggest that sites of FW2 action may originate or be located at the bacterial membrane.

To validate this hypothesis, the affinity of FW2 for LPS and LTA was initially assessed. This evaluation was based on the potential electrostatic interactions between positively charged Arg residues in FW2 and negatively charged LPS and LTA. The results indicated that at a concentration of 2 μM, FW2 exhibited strong binding capacity to both LPS and LTA, displaying concentration-dependent behavior (Fig. 4b and 4b-1). Subsequently, the permeability of FW2 to the distinctive membrane components of *E. coli* ATCC 25922 and *S. aureus* ATCC 29213 were investigated. The OM provides added protection against Gram-negative bacteria [45]. As the concentration increased, FW2 gradually enhanced OM permeability, reaching 100 % at 16 μM (Fig. 4c). Peptidoglycan (PG) constitutes a primary component of the cell wall in Gram-positive bacteria [60]. Following 1h co-incubation of free PG (32 μM) with FW2 (1 × MBC), the death rate of *S. aureus* ATCC 29213 decreased to below 30 % and declined further at increased concentrations (Figs. 4c–1). This suggests a robust electrostatic attraction between FW2 and PG. The combination of micellar molecules and negatively charged components has the potential to disrupt the fluidity and permeability of lipid bilayers or the density of lipid packing [61,62]. Hence, the membrane fluidity-sensitive dye Laurdan GP was used to assess if FW2 altered the membrane fluidity of *E. coli* or *S. aureus*. With increasing local FW2 concentration, a significant enhancement in Laurdan GP fluorescence intensity at 4 μM, indicating reduced membrane fluidity of *E. coli* ATCC 25922 (Fig. 4d). In contrast, in *S. aureus* ATCC 29213, an inverse trend was observed, in which the Laurdan GP fluorescence intensity significantly decreased in the presence of FW2 at 2 μM concentration (Figs. 4d–1). This effect is similar to that of the well-known membrane fluidizer benzyl alcohol (BA), suggesting its ability to elevate the membrane fluidity of *S. aureus* bacteria [46,63]. When confronted with external threats, both Gram-positive and Gram-negative bacteria are likely to initiate diverse self-protective mechanisms, adjusting

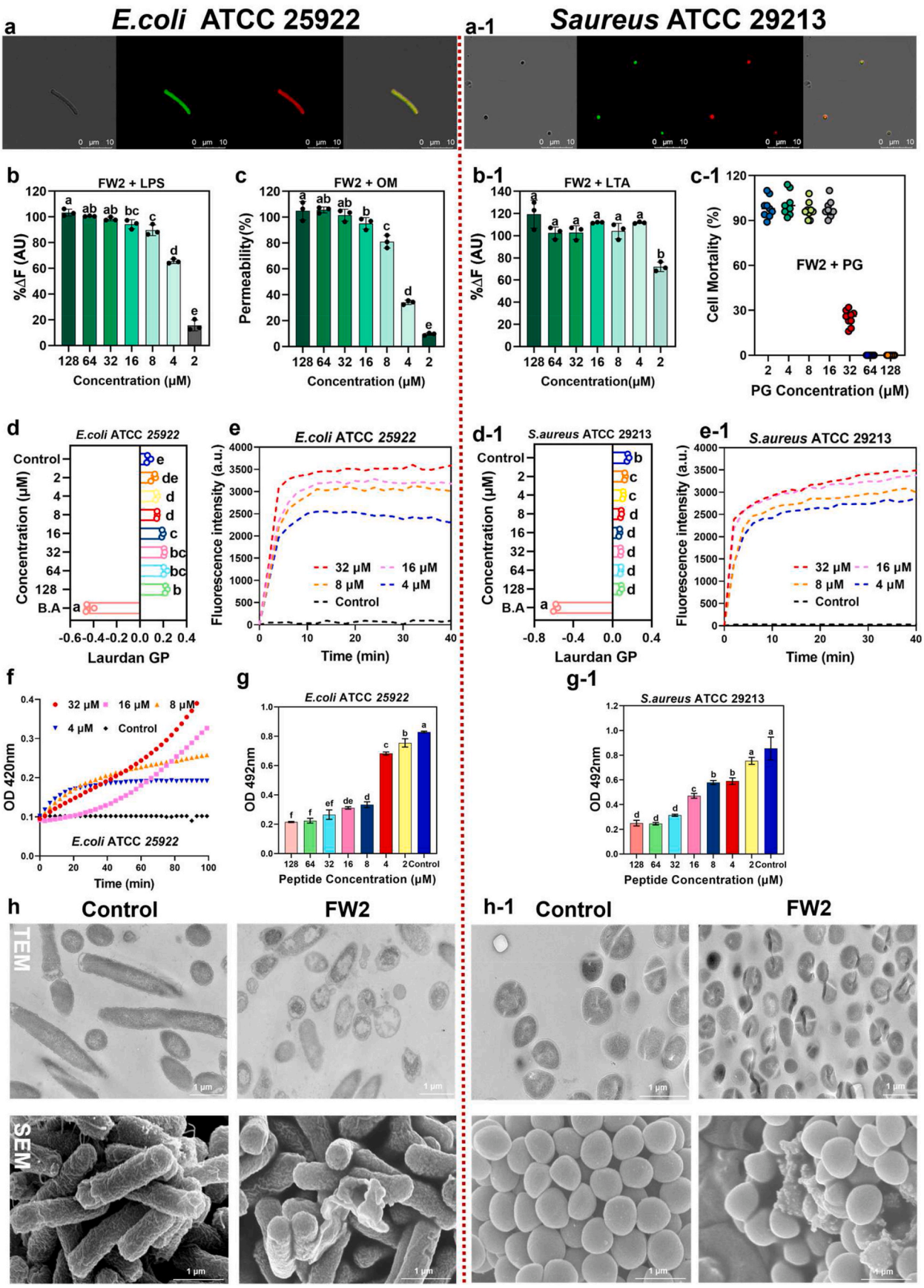

(caption on next page)

Fig. 4. **(a)** CLSM observations for *E. coli* ATCC 25922 and **(a-1)** *S. aureus* ATCC 29213. Green signal: FITC-label, red signal: PI. **(b)** LPS binding affinities and **(b-1)** LTA binding affinities at different concentrations of peptides. The error bars indicate the SDs derived from the mean of three separate and independent replicates. **(c)** The permeability of the OM was assessed using NPN following to exposure to FW2 (mean ± SD, n = 3). **(c-1)** Cell mortality rate of *S. aureus* ATCC 29213 were incubated with free PG and FW2 (1 × MBC). The experiment was independently repeated three times, with three replicates each time. **(d)** Laurdan GP was used to assess the membrane fluidity of *E. coli* ATCC 25922 and **(d-1)** *S. aureus* ATCC 29213 treated with FW2. Results are given as the mean ± SD (n = 3). **(e)** Cytoplasmic membrane depolarization of *E. coli* ATCC 25922 and **(e-1)** *S. aureus* ATCC 29213 induced by FW2 at different concentrations. **(f)** IM of *E. coli* ATCC 25922 permeability induced by FW2. **(g)** Inhibitory effect on respiratory chain dehydrogenase of *E. coli* ATCC 25922 and **g-1)** *S. aureus* ATCC 29213 induced by FW2, mean ± SD (n = 3). **(h)** TEM and SEM images of *E. coli* and **(h-1)** *S. aureus* after treatment with FW2 at 37 °C for 1 h, Scale bar = 1.00 μm. Variations among cohorts exposed to different concentrations were assessed using one-way ANOVA and subsequent Tukey's post hoc analysis. Dissimilarities identified by distinct superscripts (a, b, and c) indicate statistically significant differences ($P < 0.05$).

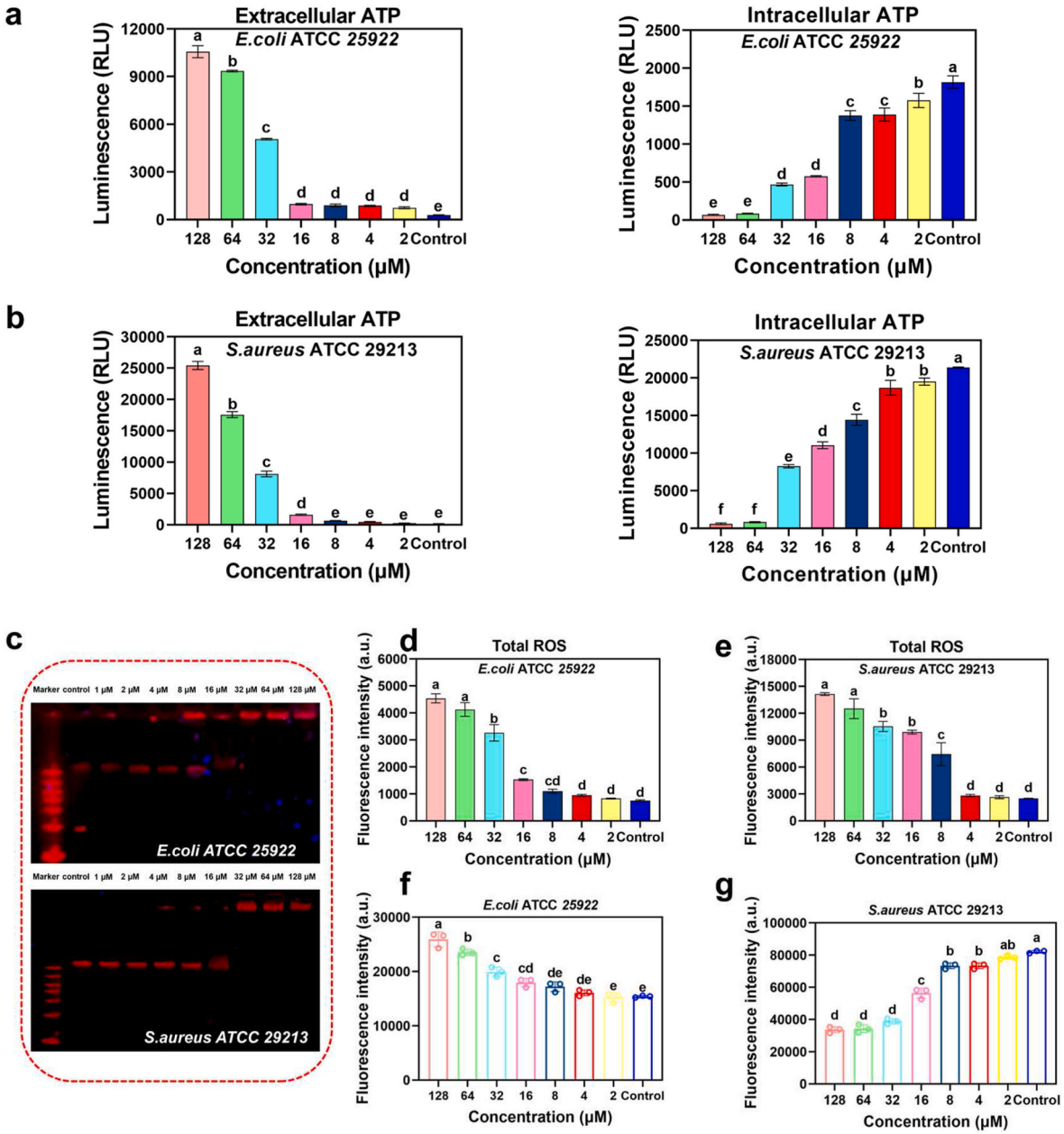

Fig. 5. **(a)** Extracellular ATP leakage and intracellular ATP levels following treatment with FW2 in *E. coli* and **(b)** *S. aureus*, (mean ± SD, n = 3). **(c)** Determination of the DNA binding ability of FW2 using the gel retardation method. DNA ladder from were as follows: 12000, 8000, 6000, 5000, 4000, 3000 and 2000 bp. Peptide concentrations were 1, 2, 4, 8, 16, 32, 64 and128 μM. Different concentrations of FW2 were incubated with genomic DNA at 37 °C for 1 h. **(d)** Different concentrations of FW2 induced ROS levels of *E. coli* ATCC 25922 and **(e)** *S. aureus* ATCC 29213, (mean ± SD, n = 3). **(f)** Changes in the intracellular pH of *E. coli* ATCC 25922 and **(g)** *S. aureus* ATCC 29213 after FW2 treatment. The dissimilarities by distinct superscripts (a, b, and c) indicate statistically significant differences with each group ($P < 0.05$).

membrane rigidity or flexibility to regulate membrane damage or uncontrolled ion channel repair [46,62]. Owing to the aggregative intrusion of micellar molecules, the bacterial membrane potential of *E. coli* and *S. aureus* experiences significant disruption, with time and dose dependency (Fig. 4e and 4e-1). A rapid increase in fluorescence intensity was observed within 5 min, followed by a subsequent plateau. Micellar molecules penetrated the IM of *E. coli*, as indicated by an increase in absorbance at OD_{420}, which signifies the release of *β*-galactosidase outside the cell membrane, correlating positively with time points, suggesting that FW2 eventually disrupts the IM of *E. coli* (Fig. 4f). As the bacterial respiratory chain resides in the cell membrane, it is speculated that the attack of FW2 may further impact the bacterial respiration process. As depicted in Fig. 4g and 4g-1, irrespective of whether *E. coli* ATCC 25922 or *S. aureus* ATCC 29213, increasing the FW2 concentration, significantly inhibits the activity of respiratory chain dehydrogenases. This suggests that when the self-assembling peptide comes into contact with the bacterial membrane, the steady state of the membrane is perturbed by affecting the activity of respiratory chain dehydrogenases, leading to the paralysis of the bacterial membrane, and consequently disrupting the balance of electron transfer in the respiratory chain.

To qualitatively investigate the mechanistic correlation, TEM and SEM were used to analyze alterations in the internal and external morphology of *E. coli* and *S. aureus* cells pre- and post-FW2 treatment, aiming to enhance the comprehension of the mechanisms of action. As revealed in Fig. 4h and **4h-1**, TEM images clearly showed the bacterial membranes and cytoplasm, whereas the SEM images exhibited a uniform surface in all bacterial samples. Post-FW2 treatment, TEM imaging exhibited cytoplasmic content leakage, bleb formation, vacuolization, and morphological alterations. SEM analysis revealed crumpled cells and fragmented structures. These observations substantiate the membrane-disruption induced by FW2.

3.5. Induction of further bacteria death signals by self-assembling peptide FW2

The damage mediated by membrane effects allowed us to penetrate the cell interior and investigate the signals associated with cell death. Due to the disruption of overall bacterial respiration, FW2 causes intracellular ATP leakage to some extent in a dose-dependent manner, indicating the inhibition of energy metabolism processes (Fig. 5a and b). Subsequently, FW2 bound to the bacterial genomic DNA, as evidenced by a reduction in DNA migration rates observed in agarose gel electrophoresis assays (Fig. 5c). This suggests the potential involvement of FW2 in the internalization of bacterial cells [64]. An increase in intracellular ROS levels and pH alterations eventually signify bacterial apoptosis (Fig. 5d–g). Similar to other antibiotics, the breakdown of membrane homeostasis tends to induce oxidative stress, facilitating ROS accumulation, leading to changes in intracellular pH and promoting cellular apoptosis [65].

Based on the aforementioned observations, we hypothesize that the primary antimicrobial mechanism of FW2 may involve both damaging the bacterial cell membrane and triggering a supplementary pathway of bacterial apoptotic signals, collectively driving the process of bacterial apoptosis.

3.6. In vivo biocompatibility and efficacy of FW2

The progressively clearer understanding of the in vitro biological activity, biocompatibility, and mechanistic analysis of the self-assembled peptide FW2, prompted our transition to explore its antibacterial effects *in vivo*. First, multiple concentration gradients of FW2 solution (5, 10, 20 mg/kg) were injected into 4 – 6-week-old female ICR mice to evaluate its safety, including assessment of locomotor activity scores and a series of associated indicators. Within 30 min of high dosage (20 mg/kg), FW2 administration, all mice exhibited signs of listlessness, huddling, and closed eyes. This behavior returned to normal within 2 h, but no such effects were observed in the medium and low dosage groups (Fig. S11). This indicates that high drug doses only provide transient stimuli to mouse organs and tissues. Each group of six mice was monitored for three days after receiving a single-dose/day intraperitoneal injection of FW2 (Fig. 6a). The weight of mice in all groups showed an upward trend with ad libitum access to food and water (Fig. 6b). Additionally, no significant differences were observed in the organ indices of the liver, spleen, and kidney among the groups ($P > 0.05$) (Fig. 6c), indicating that FW2 at the tested concentration did not exhibit significant accumulative organ toxicity in mice. Parameters such as alkaline phosphatase (ALP), Alanine aminotransferase (ALT), blood urea nitrogen (BUN), creatinine (CREA), and total bilirubin (TBIL) showed no significant differences ($P > 0.05$), indicating that FW2 did not cause liver or kidney damage (Fig. 6d). Furthermore, no apparent pathological changes were observed in H&E staining for histological examination (Fig. S12).

The efficacy of FW2 in an acute peritonitis mouse model was further investigated *in vivo*. Susceptibility of *E. coli* to FW2 and gentamicin was assessed before systemic challenge in mice. Over 25 days, gentamicin resistance was demonstrated on the fifth day, with the MIC value increasing 64-fold by the 23rd day, however, FW2 did not result in increased resistance (Fig. 6e). This indicates that the unique membrane mechanism of FW2 can replace antibiotics that are becoming ineffective in the future. Subsequently, appropriate doses were determined based on the mortality status of mice 24 h after infection. Mice were intraperitoneally injected with 100 μL of *E. coli* ($OD_{600} = 0.3$), followed by single treatments with FW2 (10 mg/kg) and gentamicin (3 mg/kg) at 1 and 4 h post-infection (Fig. 6f). FW2 and gentamicin effectively alleviate the systemic inflammatory response induced by *E. coli*, resulting in a significant reduction in the levels of proinflammatory cytokines, including IL-1β, IL-6, and TNF-α (Fig. 6g).

H&E staining revealed hepatocyte degeneration, hepatic cord loss, blurred splenic sinus tissue with significant infiltration of inflammatory cells, and morphological atrophy and fragmentation of renal tubules in the infected group (Fig. 6h). In comparison, tissue damage exhibited varying degrees of alleviation following treatment with FW2 and gentamicin. Finally, FW2 treatment significantly reduced of bacterial burden in the peritoneal cavity, liver, spleen, and kidney, confirming its efficacy in *in vivo* applications (Fig. 6i).

4. Conclusion

Compared to complex synthetic procedures and non-natural component hydrophobic groups, there is a relative scarcity in the development of self-assembly directions exclusively using naturally occurring amino acid short peptide templates and conducting a systematic analysis of their biological effectiveness. This study employed a bola-based structural framework and fine-tuned sequences with terminally anchored hydrophobic amino acids to construct MDPs exhibiting high stability and antibacterial functionality. The study also examined the impact of terminally anchored Phe and Trp, along with the hydrophobic structure of the molecular center, on the secondary structure and antibacterial activity of the peptides. The target peptide FW2, selected through a series of biological functionality screenings, exhibited the highest selectivity index and can form micelles in aqueous media without the addition of any exogenous additives. FW2 has the advantages of low cytotoxicity and high stability and exhibits minor variations in antibacterial activity in the presence of serum and salt ions. FW2 induces bacterial apoptosis by disrupting bacterial cell membranes and employing multiple bactericidal mechanisms. Additionally, FW2 exhibits favorable *in vivo* biocompatibility, effectively treating bacterial infections *in vivo*. These findings represent the application of optimized MDPs in the design of novel antimicrobials. This may accelerate the translation of antibacterial biomaterials for clinical applications or animal husbandry field by systematic analysis of their biological functions.

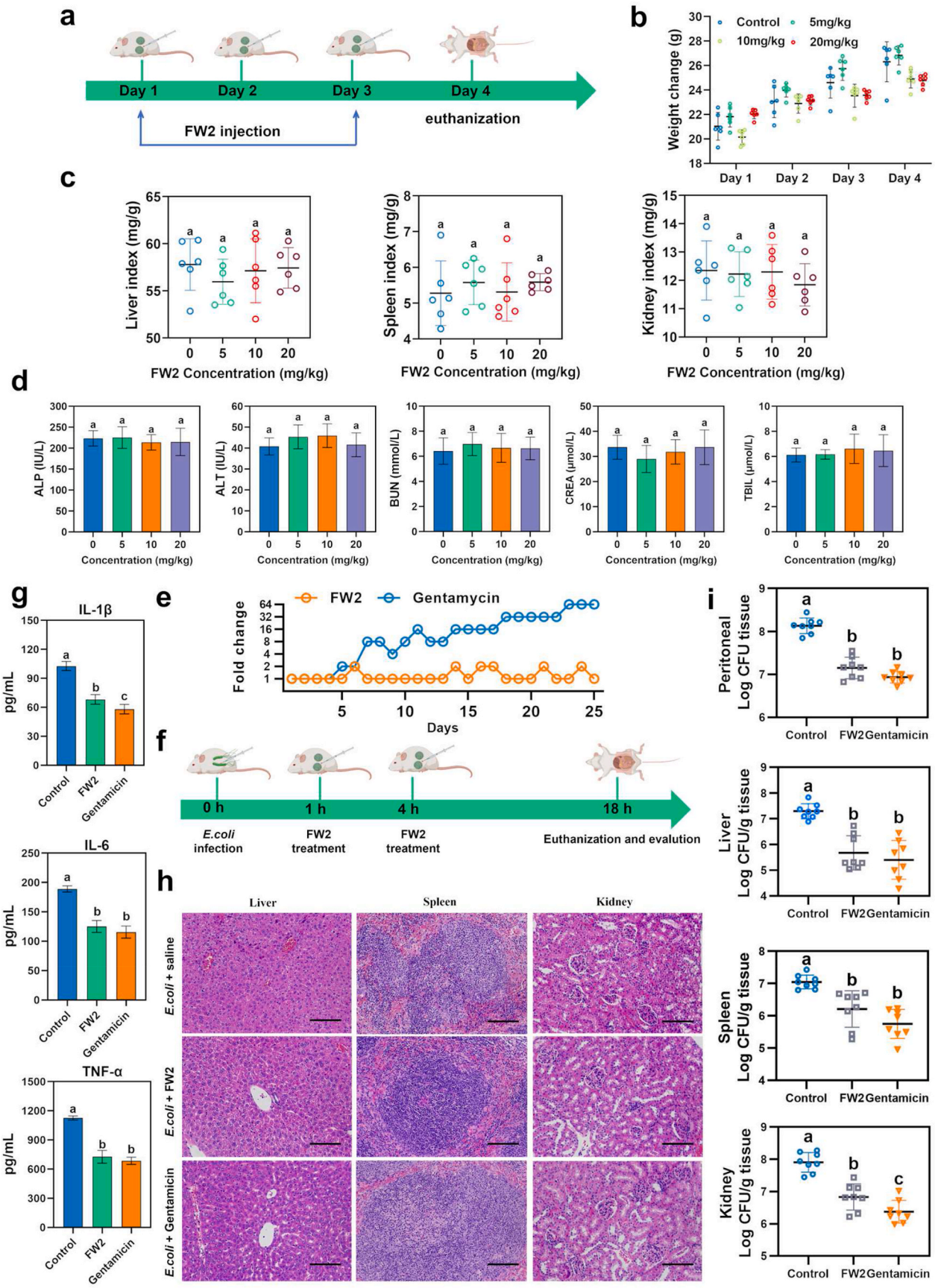

(caption on next page)

Fig. 6. **(a)** Schematic of the biocompatibility measurement protocol. **(b)** Weight curve alterations and **(c)** Relative organ index (mean ± SD, n = 6). **(d)** Hepatic and renal function tests were conducted on mice receiving multiple doses of FW2. The outcomes are presented as the mean ± SD (n = 6). **(e)** Development of FW2 and gentamycin resistance to *E. coli* culture for 25 days. **(f)** *In vivo* program of FW2 (10 mg/kg) and gentamycin (3 mg/kg) treatment of ICR mice. **(g)** Effects of FW2 on the IL-1β, IL-6, and TNF-α levels in mouse serum. Data are presented as mean ± SD (n = 8). **(h)** Histopathological morphology of the liver, spleen, and kidney tissue from infected, FW2-treated, and gentamicin-treated mice. Scale bar = 100 μm. **(i)** Fluctuations in bacterial load within the peritoneal cavity, liver, spleen, and kidney tissue samples after infection and the administration of FW2 and gentamicin. Data presented as the mean ± SD (n = 8). *P* values were calculated using one-way ANOVA with Tukey's multiple comparisons test. Significant differences ($P < 0.05$) between groups are denoted by different superscripted letters (a, b, c).

Funding

This work was supported by the National Key R&D Program of China (2022YFD1300700), the National Natural Science Foundation of China (Nos. 32030101, 32272914, and 32002215), Heilongjiang Provincial Collaborative Innovation Achievement Project for Universities - Incubation Project (LJGXCG2022-022), and the Heilongjiang Touyan Innovation Team Program (No.54600112).

CRediT authorship contribution statement

Weikang Yu: Writing – original draft, Methodology, Investigation, Formal analysis, Data curation, Conceptualization. **Xu Guo:** Software, Formal analysis, Validation. **Xuefeng Li:** Software, Supervision, Visualization. **Yingxin Wei:** Software, Supervision. **Yinfeng Lyu:** Methodology, Resources, Visualization. **Licong Zhang:** Formal analysis, Project administration. **Jiajun Wang:** Funding acquisition, Validation, Writing – review & editing. **Anshan Shan:** Conceptualization, Data curation, Funding acquisition, Project administration, Writing – review & editing.

Declaration of competing interest

The authors declare that they have no known competing financial interests or personal relationships that could have appeared to influence the work reported in this paper.

Data availability

Data will be made available on request.

Appendix A. Supplementary data

Supplementary data to this article can be found online at https://doi.org/10.1016/j.mtbio.2024.101183.

References

[1] Y.E. Gencay, D. Jasinskyté, C. Robert, et al., Engineered phage with antibacterial CRISPR-Cas selectively reduce burden in mice, Nat. Biotechnol. 42 (2024) 23.
[2] X. Dong, J. Ye, Y. Chen, et al., Intelligent peptide-nanorods against drug-resistant bacterial infection and promote wound healing by mild-temperature photothermal therapy, Chem. Eng. J. 432 (2022) 12.
[3] D.M. Whiley, J.A. Tickner, R.L. Kundu, et al., Selection of ceftriaxone resistance using doxycycline post-exposure prophylaxis, Lancet Infect. Dis. 23 (2023) E268–E269.
[4] M. Baym, L.K. Stone, R. Kishony, Multidrug evolutionary strategies to reverse antibiotic resistance, Science 351 (2016) 5.
[5] P.J. Yeh, M.J. Hegreness, A.P. Aiden, et al., Systems microbiology - opinion drug interactions and the evolution of antibiotic resistance, Nat. Rev. Microbiol. 7 (2009) 460–466.
[6] X. Hou, X. Zhang, W. Zhao, et al., Vitamin lipid nanoparticles enable adoptive macrophage transfer for the treatment of multidrug-resistant bacterial sepsis, Nat. Nanotechnol. 15 (2020) 41–46.
[7] Y. Xie, X. Qin, J. Zhang, et al., Self-assembly of peptide nanofibers with chirality-encoded antimicrobial activity, J. Colloid Interface Sci. 622 (2022) 135–146.
[8] X. Fang, H. Liu, Y. Du, et al., Bacillus siamensis targeted screening from high colitis-resistant pigs can alleviate ulcerative colitis in mice, Research, https://doi.org/10.34133/research.0415, 2024.
[9] Q. Gao, M. Yu, Y. Su, et al., Rationally designed dual functional block copolymers for bottlebrush-like coatings: n vitro and in vivo antimicrobial, antibiofilm, and antifouling properties, Acta Biomater. 51 (2017) 112–124.
[10] N.D.T. Tram, J. Xu, D. Mukherjee, et al., Bacteria-responsive self-assembly of antimicrobial peptide nanonets for trap-and-kill of antibiotic-resistant strains, Adv. Funct. Mater. 33 (2023) 14.
[11] V. Armiento, K. Hille, D. Naltsas, et al., The human host-defense peptide cathelicidin LL-37 is a nanomolar inhibitor of amyloid self-assembly of islet amyloid polypeptide (IAPP), Angew. Chem.-Int. Edit. 59 (2020) 12837–12841.
[12] P. Szymczak, M. Możejko, T. Grzegorzek, et al., Discovering highly potent antimicrobial peptides with deep generative model HydrAMP, Nat. Commun. 14 (2023) 23.
[13] Y. Di, Q. Lin, C. Chen, et al., Enhanced therapeutic index of an antimicrobial peptide in mice by increasing safety and activity against multidrug-resistant bacteria, Sci. Adv. 6 (2020) 10.
[14] W. Yu, Y. Sun, W. Li, et al., Self-assembly of antimicrobial peptide-based micelles breaks the limitation of trypsin, ACS Appl. Mater. Interfaces 15 (2022) 494–510.
[15] Y. Zhu, M.U. Akhtar, B. Li, et al., The design of cell-selective tryptophan and arginine-rich antimicrobial peptides by introducing hydrophilic uncharged residues, Acta Biomater. 153 (2022) 557–572.
[16] N. Gao, J. Wang, C. Fang, et al., Combating bacterial infections with host defense peptides: shifting focus from bacteria to host immunity, Drug Resist, Update 72 (2024) 101030.
[17] Y. Fang, L. Li, M. Sui, et al., Protein transduction system based on tryptophan-zipper against intracellular infections via inhibiting ferroptosis of macrophages, ACS Nano 17 (2023) 12247–12265.
[18] W. Yu, J. Wang, Z. Wang, et al., PEGylation of the antimicrobial peptide PG-1: a link between propensity for nanostructuring and capacity of the antitrypsin hydrolytic ability, J. Med. Chem. 64 (2021) 10469–10481.
[19] Z. Lai, Q. Jian, G. Li, et al., Self-assembling peptide dendron nanoparticles with high stability and a multimodal antimicrobial mechanism of action, ACS Nano 15 (2021) 15824–15840.
[20] T. Chen, Y. Lyu, M. Tan, et al., Correction to "fabrication of supramolecular antibacterial nanofibers with membrane-disruptive mechanism", J. Med. Chem. 65 (2021), 888-888.
[21] Y. Fan, X. Li, P. He, et al., A biomimetic peptide recognizes and traps bacteria in vivo as human defensin-6, Sci. Adv. 6 (2020) eaaz4767.
[22] Y. Fang, Y. Zhu, L. Li, et al., Biomaterial-interrelated bacterial sweeper: simplified self-assembled octapeptides with double-layered trp zipper induces membrane destabilization and bacterial apoptosis-like death, Small Methods 5 (2021) e2101304.
[23] G. Li, Z. Lai, A. Shan, Advances of antimicrobial peptide-based biomaterials for the treatment of bacterial infections, Adv. Sci. 10 (2023) e2206602.
[24] W. Dong, Z. Liu, L. Sun, et al., Antimicrobial activity and self-assembly behavior of antimicrobial peptide chensinin-1b with lipophilic alkyl tails, Eur. J. Med. Chem. 150 (2018) 546–558.
[25] G. Yang, T. Huang, Y. Wang, et al., Sustained release of antimicrobial peptide from self-assembling hydrogel enhanced osteogenesis, J. Biomater. Sci.-Polym 29 (2018) 1812–1824.
[26] C.D. Spicer, C. Jumeaux, B. Gupta, et al., Peptide and protein nanoparticle conjugates: versatile platforms for biomedical applications, Chem. Soc. Rev. 47 (2018) 3574–3620.
[27] F. Peng, Y. Chen, J. Liu, et al., Facile design of gemini surfactant-like peptide for hydrophobic drug delivery and antimicrobial activity, J. Colloid Interface Sci. 591 (2021) 314–325.
[28] J. Li, J. Wang, Y. Zhao, et al., Surfactant-like peptides: from molecular design to controllable self-assembly with applications, Coord. Chem. Rev. 421 (2020) 15.
[29] C. Chen, J. Hu, S. Zhang, et al., Molecular mechanisms of antibacterial and antitumor actions of designed surfactant-like peptides, Biomaterials 33 (2012) 592–603.
[30] I.W. Hamley, Peptide nanotubes, Angew. Chem.-Int. Edit. 53 (2014) 6866–6881.
[31] C.J.C. Edwards-Gayle, V. Castelletto, I.W. Hamley, et al., Self-assembly, antimicrobial activity, and membrane interactions of arginine-capped peptide bola-amphiphiles, ACS Appl. Bio Mater. 2 (2019) 2208–2218.
[32] L.R. Mello, R.B. Aguiar, R.Y. Yamada, et al., Amphipathic design dictates self-assembly, cytotoxicity and cell uptake of arginine-rich surfactant-like peptides, J. Mater. Chem. B 8 (2020) 2495–2507.
[33] K. Yamauchi, Y. Sakamoto, A. Moriya, et al., Archaebacterial lipid models. Highly thermostable membranes from 1,1'-(1,32-dotriacontamethylene)-bis(2-phytanyl-sn-glycero-3-phosphocholine), J. Am. Chem. Soc. 112 (2002) 3188–3191.
[34] R. Sunil Singh, Supramolecular gels from bolaamphiphilic molecules, J. Mol. Liq. 394 (2024) 30.
[35] F. Tian, R. Guo, C. Wu, et al., Assembly of glycopeptides in living cells resembling viral infection for cargo delivery, Angew. Chem.-Int. Edit. 13 (2024).
[36] M. Niu, X. Gu, J. Yang, et al., Dual-mechanism glycolipidpeptide with high antimicrobial activity, immunomodulatory activity, and potential application for combined antibacterial therapy, ACS Nano 17 (2023) 6292–6316.
[37] S. He, Z. Yang, X. Li, et al., Boosting stability and therapeutic potential of proteolysis-resistant antimicrobial peptides by end-tagging β-naphthylalanine, Acta Biomater. 164 (2023) 175–194.
[38] D.A. Dougherty, Cation-π interactions in chemistry and biology: a new view of benzene, phe, tyr, and trp, Science 271 (1996) 163–168.

[39] Q. Li, J. Li, W. Yu, et al., De novo design of a pH-triggered self-assembled β-hairpin nanopeptide with the dual biological functions for antibacterial and entrapment, J. Nanobiotechnol. 19 (2021) 183.
[40] C. Wang, C. Shao, Y. Fang, et al., Binding loop of sunflower trypsin inhibitor 1 serves as a design motif for proteolysis-resistant antimicrobial peptides, Acta Biomater. 124 (2021) 254–269.
[41] C. Shao, Y. Wang, G. Li, et al., Novel design of simplified β-hairpin antimicrobial peptide as a potential food preservative based on trp-pocket backbone, Food Chem. 448 (2024) 13.
[42] W. Yu, X. Guo, Q. Li, et al., Revolutionizing antimicrobial biomaterials: integrating an enzyme degradation-resistant sequence into self-assembled nanosystems to overcome stability limitations of peptide-based drugs, Adv. Fiber Mater. (2024), https://doi.org/10.1007/s42765-024-00410-y.
[43] C. Shao, H. Tian, T. Wang, et al., Central β-turn increases the cell selectivity of imperfectly amphipathic α-helical peptides, Acta Biomater. 69 (2018) 243–255.
[44] Y. Lyu, M. Tan, M. Xue, et al., Broad-spectrum hybrid antimicrobial peptides derived from PMAP-23 with potential LPS binding ability, Biochem. Pharmacol. 210 (2023) 13.
[45] Y. Zhu, C. Shao, G. Li, et al., Rational avoidance of protease cleavage sites and symmetrical end-tagging significantly enhances the stability and therapeutic potential of antimicrobial peptides, J. Med. Chem. 63 (2020) 9421–9435.
[46] W. Kim, G.J. Zou, T.P.A. Hari, et al., A selective membrane-targeting repurposed antibiotic with activity against persistent methicillin-resistant, P Natl Acad Sci USA 116 (2019) 16529–16534.
[47] Z. Wang, Q. Li, J. Li, et al., pH-responsive antimicrobial peptide with selective killing activity for bacterial abscess therapy, J. Med. Chem. 65 (2022) 5355–5373.
[48] Z. Lai, P. Tan, Y. Zhu, et al., Highly stabilized α-helical coiled coils kill gram-negative bacteria by multicomplementary mechanisms under acidic condition, ACS Appl. Mater. Interfaces 11 (2019) 22113–22128.
[49] C. Shao, Q. Jian, B. Li, et al., Ultrashort all-hydrocarbon stapled α-helix amphiphile as a potent and stable antimicrobial compound, J. Med. Chem. 66 (2023) 11414–11427.
[50] W. Wu, J. Song, T. Li, et al., Unlocking antibacterial potential: key-site-based regulation of antibacterial spectrum of peptides, J. Med. Chem. 67 (2024) 4131–4149.
[51] S.J. Lam, N.M. O'Brien-Simpson, N. Pantarat, et al., Combating multidrug-resistant gram-negative bacteria with structurally nanoengineered antimicrobial peptide polymers, Nature Microbiol 1 (2016) 16162.
[52] J.S. Khara, S. Obuobi, Y. Wang, et al., Disruption of drug-resistant biofilms using designed short α-helical antimicrobial peptides with idealized facial amphiphilicity, Acta Biomater. 57 (2017) 103–114.
[53] B. Xu, W. Shaoyong, L. Wang, et al., Gut-targeted nanoparticles deliver specifically targeted antimicrobial peptides against infections, Sci. Adv. 9 (2023) eadf8782.
[54] Z. Wang, Q. Li, J. Li, et al., The trp-rich antimicrobial amphiphiles with intramolecular aromatic interactions for the treatment of bacterial infection, Front. Microbiol. 12 (2021) 17.
[55] R.M. Epand, C. Walker, R.F. Epand, et al., Molecular mechanisms of membrane targeting antibiotics, BBA-Biomembranes 1858 (2016) 980–987.
[56] M. Slyngborg, P. Fojan, A computational study of the self-assembly of the RFFFR peptide, Phys, Chem. Chem. Phys. 17 (2015) 30023–30036.
[57] X. Dou, X. Zhu, J. Wang, et al., Novel design of heptad amphiphiles to enhance cell selectivity, salt resistance, antibiofilm properties and their membrane disruptive mechanism, J. Med. Chem. 60 (2017) 2257–2270.
[58] B. Song, B. Liu, Y. Jin, et al., Controlled self-assembly of helical nano-ribbons formed by achiral amphiphiles, Nanoscale 7 (2015) 930–935.
[59] L. Stagi, M. Sini, D. Carboni, et al., Modulating the poly-l-lysine structure through the control of the protonation-deprotonation state of l-lysine, Sci. Rep. 12 (2022) 13.
[60] N. Malanovic, K. Lohner, Gram-positive bacterial cell envelopes: the impact on the activity of antimicrobial peptides, BBA-Biomembranes 1858 (2016) 936–946.
[61] M.L. Cartron, S.R. England, A.I. Chiriac, et al., Bactericidal Activity of the Human Skin Fatty Acid -6-hexadecanoic Acid on, 58, Antimicrob Agents Ch, 2014, pp. 3599–3609.
[62] D. Saeloh, V. Tipmanee, K.K. Jim, et al., The novel antibiotic rhodomyrtone traps membrane proteins in vesicles with increased fluidity, PLoS Pathog. 14 (2018) e1006876.
[63] T. Parasassi, M. Di Stefano, M. Loiero, et al., Influence of cholesterol on phospholipid bilayers phase domains as detected by Laurdan fluorescence, Biophys. J. 66 (1994) 120–132.
[64] J. Nam, H. Yun, G. Rajasekaran, et al., Structural and functional assessment of mBjAMP1, an antimicrobial peptide from branchiostoma japonicum, revealed a novel α-hairpinin-like scaffold with membrane permeable and DNA binding activity, J. Med. Chem. 61 (2018) 11101–11113.
[65] X. Zhao, M. Zhang, I. Muhammad, et al., An antibacterial peptide with high resistance to trypsin obtained by substituting d-amino acids for trypsin cleavage sites, Antibiotics-Basel 10 (2021) 20.